

Micro-tomography based analysis of thermal conductivity, diffusivity and oxidation behavior of rigid and flexible fibrous insulators

Francesco Panerai^{a,b,*}, Joseph C. Ferguson^{a,c}, Jean Lachaud^d, Alexandre Martin^a, Matthew J. Gasch^e, Nagi N. Mansour^f

^a *Department of Mechanical Engineering, University of Kentucky, 151 Ralph G. Anderson Bldg., Lexington, KY 40506, USA*

^b *AMA Inc. at NASA Ames Research Center, Mail Stop 234-1, Moffett Field, CA 94035, USA.*

^b *STC at NASA Ames Research Center, Mail Stop 258-6, Moffett Field, CA 94035, USA.*

^d *Silicon Valley Initiatives, University of California Santa Cruz, NASA Ames Research Park Bldg. 19, Moffett Field, CA 94035, USA*

^c *Thermal Protection Systems and Materials Branch, NASA Ames Research Center, Mail Stop 234-1, Moffett Field, CA 94035, USA*

^c *Advanced Supercomputing Division, NASA Ames Research Center, Mail Stop 258-5, Moffett Field, CA 94035, USA*

ABSTRACT: Material properties and oxidation behavior of low-density felts used as substrates for conformal carbon/phenolic ablators were compared with those of a rigid carbon fiber preform used to manufacture heritage lightweight ablators. Synchrotron x-ray micro-tomography measurements were performed to characterize the materials' microstructure at the scale of the fibers. Using the

*Corresponding author. Tel.: +1 650 604 3075. Email address: francesco.panerai@nasa.gov (Francesco Panerai).

tomography voxels as computational grids, tortuosity in the continuum regime, and room temperature conductivity were computed. Micro-scale simulations of the oxidation of carbon fibers were carried out using a random walk model for oxygen diffusion and a sticking probability law to model surface reactions. The study shows that, due to a higher porosity and lower connectivity, the felt materials have lower thermal conductivity but a faster recession rate than that of the rigid preform. Challenges associated with computations based on micro-tomography are also discussed.

Keywords: A. Carbon fibers; B. Porosity; B. Thermal properties; B. Oxidation.

1. Introduction

The successful atmospheric entries of Stardust, Mars Science Laboratory (MSL) and the recent flights of the SpaceX Dragon capsule have demonstrated a substantial maturity and performance of lightweight carbon/phenolic thermal protection systems (TPS). This class of lightweight ablators, with densities ($\sim 0.3 \text{ g/cm}^3$) much lower than fully dense carbon/phenolic ($\sim 1.5 \text{ g/cm}^3$), has proven capable of handling the aerothermal heating over a wide range of entry speeds and in different atmospheric environments.

In order to prepare for future exploration missions and to meet the more demanding thermal protection requirements of anticipated atmospheric entries, NASA is improving material response models for low-density carbon/phenolic ablators and developing new material technologies that enable better performance and more effective design. Examples of these technologies are conformal and flexible carbon/phenolic composites [1, 2]. Their basic architecture is obtained infusing a phenolic resin into an insulating fibrous substrate, following the flight-proven state-of-the-art architecture of the Phenolic Impregnated Carbon Ablator (PICA) [3]. However, unlike PICA, which is based on a rigid preform, new materials with high application potential adopt flexible felts as the material substrate [1, 2]. Felt substrates suitable for flexible and conformal ablators are based on ceramic, polymers or

carbon fibers. An example of such technology is Conformal-PICA (also referred to as C-PICA) [1, 2], where a rayon-based carbon felt is infused with phenolic. These new materials have been successfully tested in arcjet environments at heat fluxes ranging from 50 to 385 W/cm² [1, 2].

Felt-based ablators have several advantages over classical rigid TPS materials. Most importantly, they mitigate the limited strain response of large rigid substrates. For example, the ceramic tiles used for the Space Shuttle [4] and heritage PICA, due to their brittleness, need to be manufactured as tiles of limited dimensions, as was the case for the large PICA heat shield of MSL [5]. In addition, felts based substrates have significantly larger strain-to-failure than rigid preforms enabling manufacturing in larger pieces. As such, they reduce the number of independent parts mitigating the need of gap fillers, they offer improved robustness in absorbing loads and deflections, and they allow shaping the substrate around complex geometries with the possibility of maintaining a uniform and low thermal conductivity in presence of curved surfaces [1]. In contrast, felts have drawbacks such as a limited thickness, poorer through-thickness mechanical properties compared to rigid preforms, and are less performant in shear environments.

In this work, we used tomography reconstructions to analyze and compare the material properties and oxidation response of rigid and flexible substrates that are used to engineer lightweight carbon/phenolic ablators. For this class of materials with a small phenolic content, the substrate drives the thermal properties of the composite. Hence, a better knowledge of the preform architecture and properties can lead to improvements and optimization of the thermal protection material. Moreover, past investigations have shown that for PICA-like ablators the more reactive charred matrix (due to the high surface area) decomposes faster than the preform under the effect of oxygen reactions, and the fiber of the substrate are left exposed to the incoming flow [6, 7]. Therefore, quantifying the oxidation of preform materials is important for predicting the overall heatshield performance.

The paper is structured as follows. Section 2 provides a review of the relevant literature on the use of

micro-CT for heat and mass transport computations in material structures. In section 3, we outline the use of synchrotron X-ray micro-tomography (micro-CT) to resolve the architecture of both felts and rigid preform at micron scale. Compared to a standard characterization obtained by scanning electron microscopy, micro-CT adds the possibility of resolving the material in three dimensions (3D) on voxels, and provides a digital representation of the material that can be used for numerical simulations. In section 4, a commercial toolbox was used to perform computations of materials properties, based on micro-CT digital representations of the material. We focus on diffusivity and room temperature thermal conductivity, which are important properties for ablator response simulations. Micro-CT data also enable simulations of the mass transport within the micro-structure and computations of the material permeability. This is not considered here, however we refer to a companion work on the topic [8], where we showed that Klinkenberg permeability in slip condition can be computed from micro-CT, using the direct simulation Monte Carlo method, with excellent agreement against experimental measurements [9]. In section 5, we used an in-house developed software, PuMA (Porous Materials Analysis) [10], to study the degradation of the material through oxidation. The paper conclusions (section 6) provide an outlook on the prospective use of micro-CT for computing material properties, and the response of high temperature fibrous insulations to their environment.

2. Literature review

In this work, numerical simulations were performed using 3D images from X-ray micro-CT as computational domains. The past two decades have witnessed the emergence of micro-CT as a primary characterization tool in material science. This is due to its ability to non-destructively characterize a material in 3D, while attaining spatial resolutions ranging from sub-micron to centimeter scale [11-14]. Both synchrotron and laboratory sources have become established methods of producing X-rays for micro-CT imaging. As the technique advanced, so too did development of

computational methods that use the digital representation of a micro-structure offered by micro-CT in order to compute material properties and response.

The numerical determination of the effective properties of porous media and composites from the properties of the constituting phases (e.g. the effective thermal conductivity as a function of constituents' conductivities) has been an extensively explored field for nearly a century. The works of Torquato [15, 16], Whitaker [17], Wang and Pan [18], and references therein are only a limited portion of the pertinent literature. While several computational and theoretical/analytical approaches have proven valuable in multiple applications, a clear advantage of micro-CT is access to the real microstructure on a broad range of scales is provided.

Several authors have used tomography data to simulate heat transfer in porous media [19-33]. While focused on very different applications of material science, such as composites, porous ceramics, wood, packed beds, snow, etc., most of these studies aimed to characterize the material's effective conductivity. Only a limited number of them accounted for contributions of both conductive and radiative transfer in porous structures [21, 23, 24, 29], and few of the published works focused on TPS applications, such as carbon/carbon [19] or silica/phenolic [30].

Micro-CT data have been used to compute permeability of porous structures [8, 20, 34-44] using Darcy's law under laminar, viscous, and continuum flow conditions. Some of these efforts considered modifications of Darcy's law to account for turbulent, shear and rarefied flow effects (Forchheimer, Brinkman, and Klinkenberg).

Numerous computations of diffusional transport and tortuosity [20, 45-49] are also found in the literature, focusing on the determination of effective diffusion coefficients under rarefied (high

Knudsen number[†]), continuum (low Knudsen number) or transitional regime (Bosanquet approximation). Among those studies, the works focused on fibrous TPS materials are those of Vignoles et al. [20, 46] (carbon/carbon composites), White et al. [44] on carbon/phenolic ablative materials and by our group on fibrous insulators [8].

3. Micro-tomography imaging and materials

Micro-CT measurements were performed at the Advanced Light Source (ALS) at Lawrence Berkeley National Laboratory. Synchrotron X-rays produced by the ALS beamline 8.3.2 provide images at sub-micron resolution with low noise. This capability is ideal for resolving the fibrous structure of highly porous substrates that have porous characteristic lengths of the order of tens of microns.

The tomography setup and its capabilities were described in details by MacDowell et al. [50]. In this study, tomography images were collected using a 2560×2160 pixels pco.edge 5.5 sCMOS camera (PCO, Kelheim, Germany) and an Optique Peter microscope (Optique Peter, Lentilly, France), equipped with a 10× Olympus Plan Apo objective (Mitutoyo, Kawasaki, Japan) installed behind a 20 μm LuAG scintillator. The optics provided a pixel size of 0.645 μm. All of the measurements were performed using a monochromatic X-ray beam at 18 keV, collecting a total of 1024 radiographs in each scan. Micro-CT projections were reconstructed into 3D images using the Octopus software (inCT, Aalst, Belgium) [51], and an ALS in-house interface implemented in the Fiji software [52]. Fiji was also used to filter tomography artifacts and segment the images for visualization.

[†] It is recalled that the Knudsen number is the ratio of the flow mean free path λ to the characteristic length of the medium L , which for porous materials it is often assumed to be the mean pore diameter d_p .

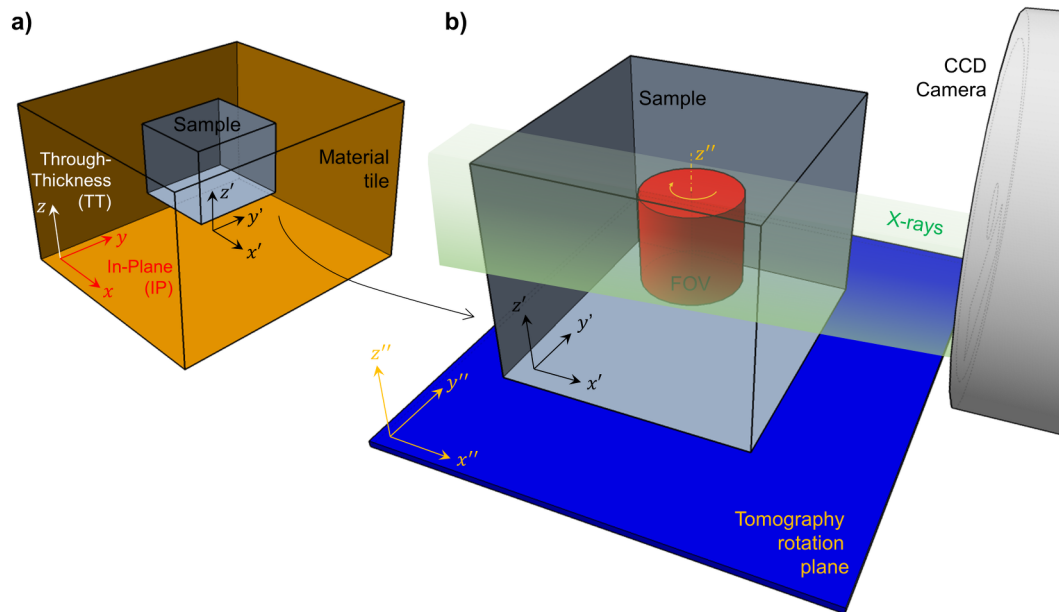


Figure 1. Schematic of a) sample extraction from material tile and b) sample positioning in the micro-CT setup. Here the xy -coordinates define the “In-Plane” (IP) direction and z the “Through-Thickness” (TT) direction of the material. $x'y'z'$ and $x''y''z''$ are the frames of reference for the sample and the tomography space, respectively. The red cylinder represents the tomography field of view (FOV), which is defined by the size of the X-ray beam and determined by the rotation of the sample.

We imaged samples of rigid carbon preform, carbon felt and rayon felt. For the rigid material, we selected FiberForm™ from Fiber Materials Inc. (Biddeford, ME, USA), the substrate used in PICA. FiberForm is made from a slurry of chopped rayon-based carbon fibers mixed with phenol-formaldehyde resin and water. The slurry is vacuum casted, compressed and cured at high temperature into desired shapes. Of the conformal and flexible materials being developed at NASA Ames Research Center (ARC) [2], two different felts were considered. We analyzed a low-density rayon-based carbon fiber felt from Morgan Advanced Material (Windsor, Cornwall, UK) and a needled (densified) rayon fiber felt from the American Felt & Filter Company (AFFCO, New Windsor, NY, USA). The rayon was made of semisynthetic fibers derived from cellulose. Felts fabrics were made by a combination of mechanical, chemical and thermal treatments that are proprietary to each manufacturer.

The manufacturing process of FiberForm confers transversely isotropic properties to material billets: the precursor material slurry is pressed along a certain direction z , causing the carbon fibers to align at $\pm 15^\circ$ angle with the xy -plane, perpendicular to the direction of compression. The process provides the material with nearly transverse isotropic properties, whereby heat and mass transport are hindered in the through-thickness (TT) direction (z) and favored along the in-plane (IP) directions (xy). Similarly, a transversely isotropic structure results from the processing of rolls and panels of felt materials. With the objective of determining material properties from 3D micro-CT images, one needs to account for errors due to extracting a sample from a billet and its positioning onto the micro-CT stage. A schematic of the preparation and placement of a sample in the imaging setup is shown in Figure 1.

In this work, efforts were made to minimize the relative rotation of the sample's frame of reference ($x'y'z'$) with respect to that of the tile (xyz) during cutting of the sample, as well as to minimize misalignments of the sample frame of reference ($x'y'z'$) with respect to that of the tomography stage ($x''y''z''$) while positioning the sample.

Photorealistic renderings of FiberForm and the carbon felt are shown in Figure 2. The visualizations were produced from triangulated micro-CT data using ray-tracing [53]. The figure highlights appreciable differences between FiberForm and the Morgan felt.

Fiber diameters ($\approx 10\text{-}12\ \mu\text{m}$) and aspect ratio of the two materials are similar, as both the fibers of the carbon felt and of FiberForm are derived from rayon. However, while FiberForm presents numerous clumps, cluster and bundles of fibers due to the FMI manufacturing process, these are not present in the felt. The carbon felt fibers appear to be organized in a more regular architecture that follows a defined pseudo-weaving pattern. This can be observed in Figure 2(b), showing a clear needling pattern.

The magnified pictures of the two materials in Figure 2(c) and (d) show two typical features of rayon fibers: a lobular cross-section and a central lumen (hollow fiber).

The felts investigated in this study were more porous than FiberForm, as can be observed from the visualization in Figure 2. An analysis of the gray-scale distribution of the tomography voxels revealed porosities of about 85 to 91% for FiberForm, while higher than $\approx 94\%$ for fibrous felts.

From the tomography images we computed a mean pore diameter of $\approx 50 \mu\text{m}$ for FiberForm and of $\approx 90 \mu\text{m}$ for the carbon felt.

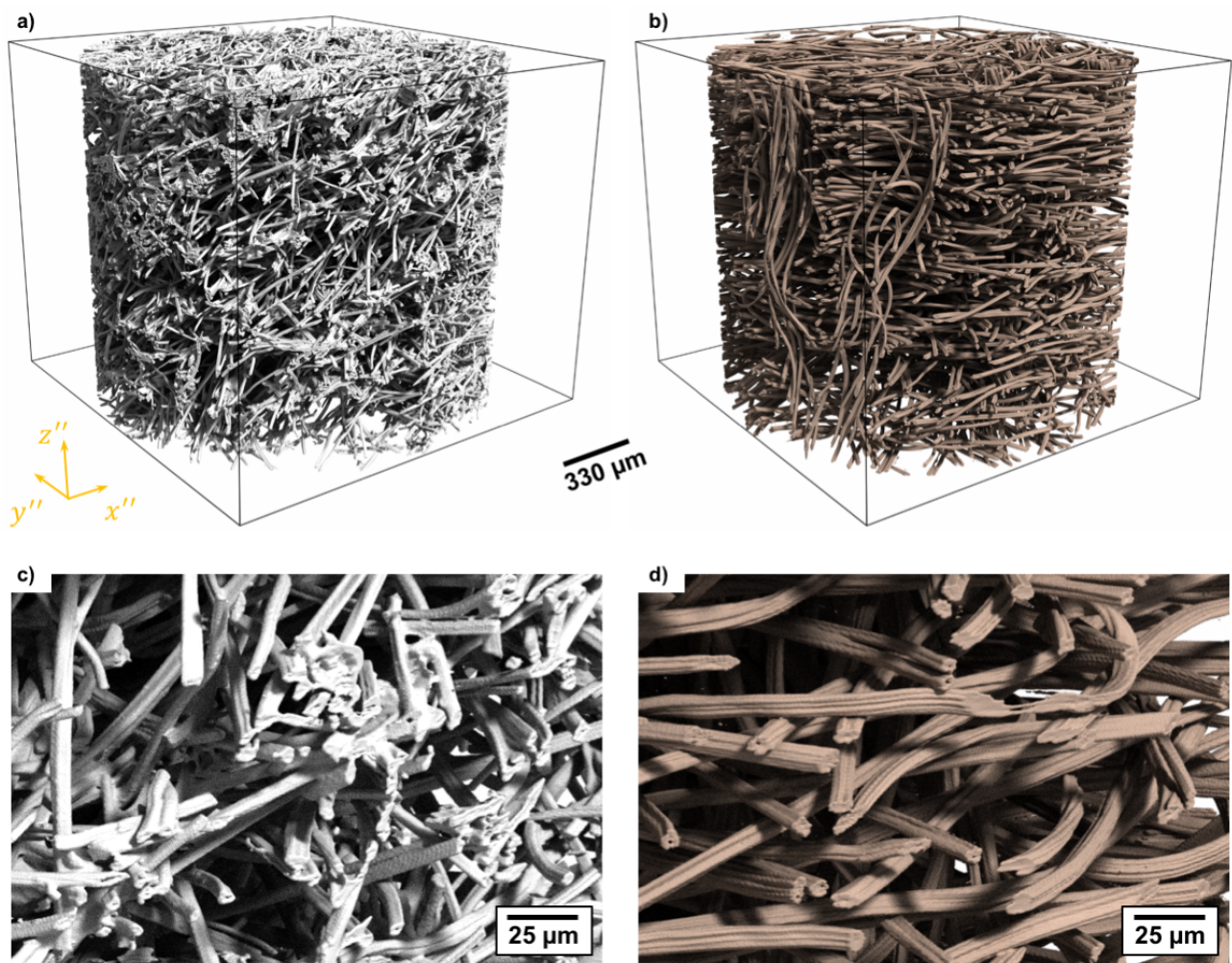


Figure 2. Micro-CT ray-tracing rendering of a) FiberForm and b) Morgan carbon fiber felt. The magnified view of the two materials (c, d) shows the typical lobular cross-section of rayon fibers and the presence of a lumen.

4. Computations of material properties

The GeoDict software [54-56] was used to perform analyses of material properties. We focused on computations of room temperature conductivity and calculations of tortuosity in the continuum regime. We also used this exercise to illustrate and discuss some of the challenges associated with micro-CT-based computations and simulations. Filtered micro-CT data were imported into the software, segmented and visualized using the OpenGL ray-casting feature of GeoDict.

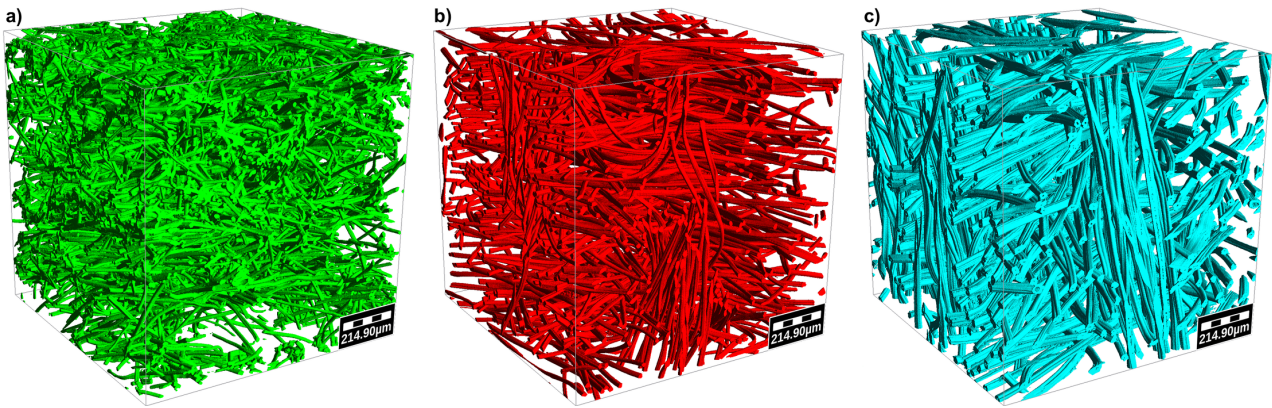


Figure 3. GeoDict computational domains from micro-CT voxels: a) FiberForm, b) carbon felt and c) rayon felt.

The computational domains used to compare the different material are presented in Figure 3 for a) FiberForm, b) carbon felt, c) needed rayon felt. As an ensemble of voxels, the micro-CT data could be used directly as a computational Cartesian grid. After segmentation, the colored voxels correspond to the fibrous material, while the white volume represents the voids between them. Prior to importing the segmented images into GeoDict, we scaled the micro-CT datasets by half (from an original voxel size of $0.645 \mu\text{m}$ to a voxel size of $1.29 \mu\text{m}$), and extracted sub-volumes of $\approx 1 \text{ mm}^3$ (800^3 voxels). Scaling the data has the advantage of allowing computations on large, representative volumes while keeping computational costs down. As an example, effective conductivity tensor calculations, performed on the half billion voxel datasets, required a computational time of the order of 1 hour using 4 threads on a workstation. Comparisons of visualizations, porosities and surface areas values of down-sampled models with the original datasets confirmed negligible loss of information and

computational errors due to voxel averaging. This is further discussed in section 4.2.

The calculations were performed in the $x''y''z''$ frame of reference of the tomography dataset. For each volume, computations allowed to determine a tensor for the generic property ξ , where the diagonal terms give the scalars of the property for the main directions of the $x''y''z''$ space.

$$\underline{\underline{\xi''}} = \begin{pmatrix} \xi''_{11} & \xi''_{12} & \xi''_{13} \\ \xi''_{21} & \xi''_{22} & \xi''_{23} \\ \xi''_{31} & \xi''_{32} & \xi''_{33} \end{pmatrix} \quad (1)$$

The matrix $\underline{\underline{\xi''}}$ is symmetric ($\xi''_{i,j} = \xi''_{j,i}$) and its off-diagonal terms are usually different from zero ($\xi''_{i \neq j} \neq 0$), unless the material microstructure is perfectly aligned with the principal directions of the physical property described by the tensor. In order to compute the principal directions for the property ξ , an eigenvalue decomposition of $\underline{\underline{\xi''}}$ is performed and the tensor is written as $\underline{\underline{\xi''}} = \underline{\underline{P}} \underline{\underline{\Lambda}} \underline{\underline{P}}^{-1}$, where $\underline{\underline{\Lambda}}$ is the diagonal matrix containing the eigenvalues λ_{ii} and $\underline{\underline{P}}$ is the rotation matrix whose columns are the eigenvectors of $\underline{\underline{\xi''}}$.

4.1. Tortuosity

For a porous medium, the tortuosity is a geometrical parameter that describes how, on average, the path of a diffusing fluid differs from a straight line. When modelling porous ablators, this parameter is important as it is used to compute the effective diffusion coefficient for the mass conservation of diffusing species [7]. The effective diffusion coefficient for a porous medium can be expressed as:

$$D_{\text{eff}} = \frac{\varepsilon}{\eta} D_{\text{ref}} \quad (2)$$

where ε is the porosity, D_{ref} is the reference diffusivity (that of the straight capillary) and η the diffusion tortuosity factor [57]. The reference diffusion coefficient reads differently depending on whether the flow is in the continuum or rarefied regime. Here, we computed tortuosity in the

continuum regime (that is, with a Knudsen number much smaller than 1), where diffusion in the pores is chiefly controlled by collisions between the molecules. Within a PICA-like ablator this flow regime may be experienced in the later portion of the trajectory, where temperatures are lower and pressures higher. In the case of a single gas, e.g. a pure O₂ flow, the reference self-diffusion coefficient can be written as $D_{\text{ref}} = \frac{1}{3}\lambda\bar{v}$ where \bar{v} is the mean thermal velocity of the gas and $\bar{\lambda}$ the mean free path of fluid particles. The DiffuDict module of GeoDict [56] was used to perform diffusion coefficients calculations for FiberForm, carbon felt and rayon felt. For the calculation of the diffusion coefficient in the continuum case, DiffuDict solves the Laplace equation, while a random walk procedure is used in the rarefied regime [56].

Continuum regime tortuosities are plotted in Figure 4. They clearly show the transversely isotropic structure of the substrates with a more tortuous path in the z direction compared to the xy direction. The larger porosity of the felt materials translates into a lower tortuosity, when compared to the tortuosity of FiberForm.

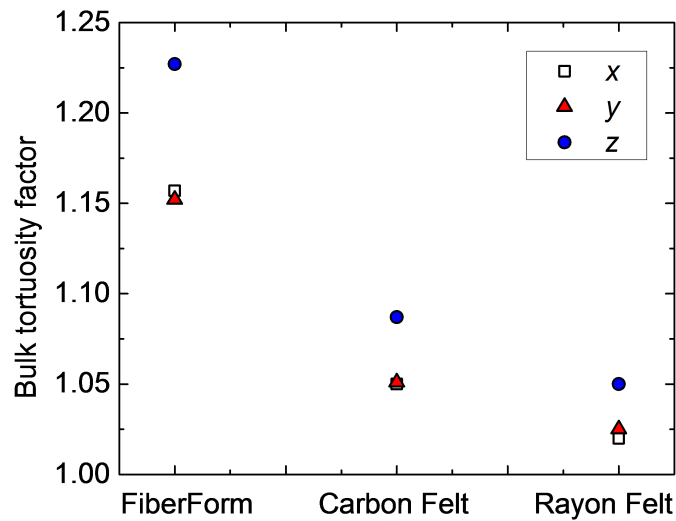


Figure 4. Continuum regime tortuosities for rigid and flexible substrates.

4.2. Room-temperature conductivity

Room-temperature conductivity computations were performed using the method described in [54].

Fourier's law was solved at steady-state for composite materials with high thermal conductivity contrast of the constituting phases [54]. Periodic boundary conditions were used and a scalar conductivity value for the different phases (carbon fibers and pores) of the material was imposed. The constituting phases were assumed to be isotropic. Radiative transfer within the porous medium was not modeled. While existing literature has highlighted the importance of radiative conductivity for FiberForm and similar insulators operating at high temperature [32, 58-61], this was an acceptable approximation for the present work, as only values at room temperature were considered.

For the simulations we adopted conductivity values published in the literature for the constituting phases (fibers and pore-filling gas). Gas conductivities are well documented in multiple sources or can be computed using available libraries [62, 63]. Choosing the conductivity for the fibers is more involved, as their conductivity depends on the composition and crystallinity. As the carbonaceous substrates investigated were both made of carbonized rayon fibers, we assumed a conductivity of $k_f = 12 \text{ W/(m}\cdot\text{K)}$ for their fibers. This assumption was based on room-temperature values for rayon-based carbon fibers found in the literature between 5 and 15 W/(m·K) [64-66]. For the conductivity of the rayon felt fibers, we used a conductivity of $k_f = 1.89 \text{ W/(m}\cdot\text{K)}$ as given in [65].

As an example, the conductivity tensor of the FiberForm sample shown in Figure 3, was computed for air at standard conditions to be:

$$\underline{\underline{\mathbf{k}}}_{FF}'' = \begin{pmatrix} 0.329 & -0.061 & -0.011 \\ -0.061 & 0.353 & -0.074 \\ -0.011 & -0.074 & 0.203 \end{pmatrix} \quad (3)$$

The value in the z direction ($k_{FF,33}'' = 0.203 \text{ W/(m}\cdot\text{K)}$) was found to be close to the nominal conductivity of 0.21 W/(m·K) of FiberForm in the transverse direction at room temperature, quoted by the manufacturer. The tensor also showed larger IP conductivities compared to the TT value.

The eigenvalue and eigenvector matrices of $\underline{\underline{\mathbf{k}}}_{FF}''$ read

$$\underline{\underline{\mathbf{k}}}_{FF} = \begin{pmatrix} 0.165 & 0 & 0 \\ 0 & 0.303 & 0 \\ 0 & 0 & 0.416 \end{pmatrix} \quad (4)$$

and

$$\underline{\underline{\mathbf{P}}}_{FF} = \begin{pmatrix} 0.215 & 0.819 & -0.532 \\ 0.418 & 0.416 & 0.808 \\ 0.883 & -0.396 & -0.253 \end{pmatrix}, \quad (5)$$

respectively. The components of the eigenvectors (columns of $\underline{\underline{\mathbf{P}}}_{FF}$) highlight the strong, local anisotropy of the materials, and provide the main directions of conduction (related to the dominant fibers' orientation) for the specific sample.

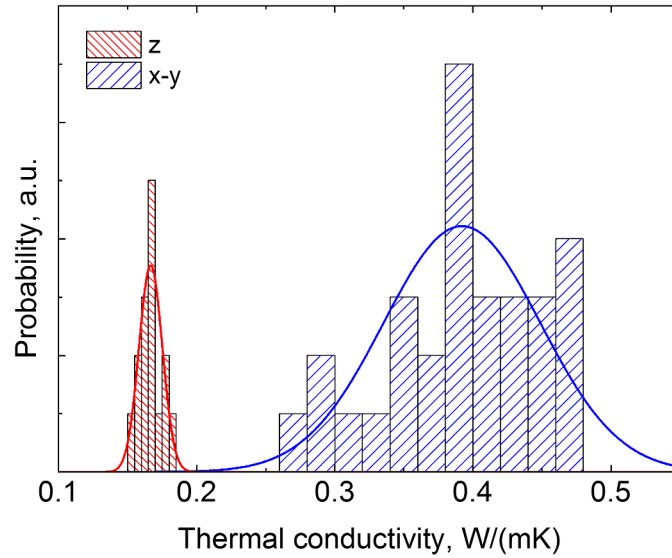


Figure 5. Normal distributions for the TT and IP conductivity of FiberForm.

To address the challenge of dealing with small volumes to analyze the properties of a materials with largely variable microstructure as FiberForm, computations were performed on multiple (fifteen) micro-CT volumes obtained imaging samples from different locations in a material billet. The results are summarized in Figure 5, where the conductivity values are fitted with standard distributions for the different directions. For the TT direction a mean conductivity was determined to be 0.167 W/(m·K) with a standard deviation of 0.008, while for the IP direction 0.392 W/(m·K) with a standard

deviation of 0.056.

It is also interesting to assess the influence of the assumption for the constituents' conductivities on the effective conductivity of the material. This was performed computing the room temperature thermal conductivity for the same FiberForm sample, for increasing values of the carbon conductivity ($k_C = 1, 2, 4, 10 \text{ W/(m}\cdot\text{K)}$), and considering the pores volume fraction as vacuum ($k_{gas} = 0 \text{ W/(m}\cdot\text{K)}$). It is shown in Figure 6 that the effective conductivity of the material scales linearly with the conductivity of its constituent phase, demonstrating that the effective conductivity is strictly a function of the geometry. Therefore, by analogy with mass diffusion transport, we can define and numerically identify the conductive tortuosity for a given architecture lying in vacuum as

$$k_{\text{eff}} = \frac{(1 - \varepsilon)}{\eta_c} k_C \quad (6)$$

Here, the conductive tortuosity η_c is not to be confused with the diffusion tortuosity factor η used in Eq. (2).

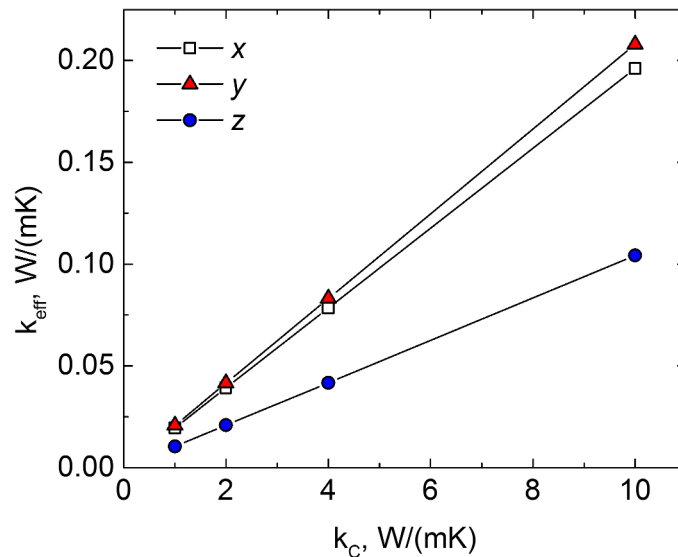


Figure 6. Variation of the effective thermal conductivity of FiberForm as a function of the carbon fibers conductivity, for a non-conductive void fraction.

One further challenge to address is related to the size of the computational domain. As mentioned

earlier, for the calculations presented in this work, we down-sampled the micro-CT samples to 800^3 voxels. A parametric study is summarized in Figure 7 where the same domain was scaled from a 1200^3 (which is nearly the maximum that we could handle with the dedicated computational resources) down to 100^3 voxels. The study was performed on FiberForm micro-CT, but same findings apply to the felt materials. The figure shows how porosity and thermal conductivity vary as the voxel size increases and information on the microstructure is progressively lost. The relative (percent) error e for the computed conductivity with respect to the 1200^3 voxels case is also presented. The figure demonstrates that, for a voxel size of $3\ \mu\text{m}$ or less, errors on the thermal conductivity computed with a scaled domain are below 10% (below 5% for the scaling used in the present study) relative to those computed with the original resolution. Therefore, it is possible to work with degraded images, still maintaining an acceptable accuracy in the computed quantities. The data shown in Figure 7 are also important as a guideline for future micro-CT measurements, namely for a trade-off between an acceptable spatial resolution and the desired field of view for the images. For FiberForm-like fibrous architectures with a typical length scale of $\sim 10\ \mu\text{m}$ (fiber diameter), if morphological details at sub-micron resolution are not of interest, the material microstructure can be well resolved with voxel sizes $\lesssim 2\ \mu\text{m}$.

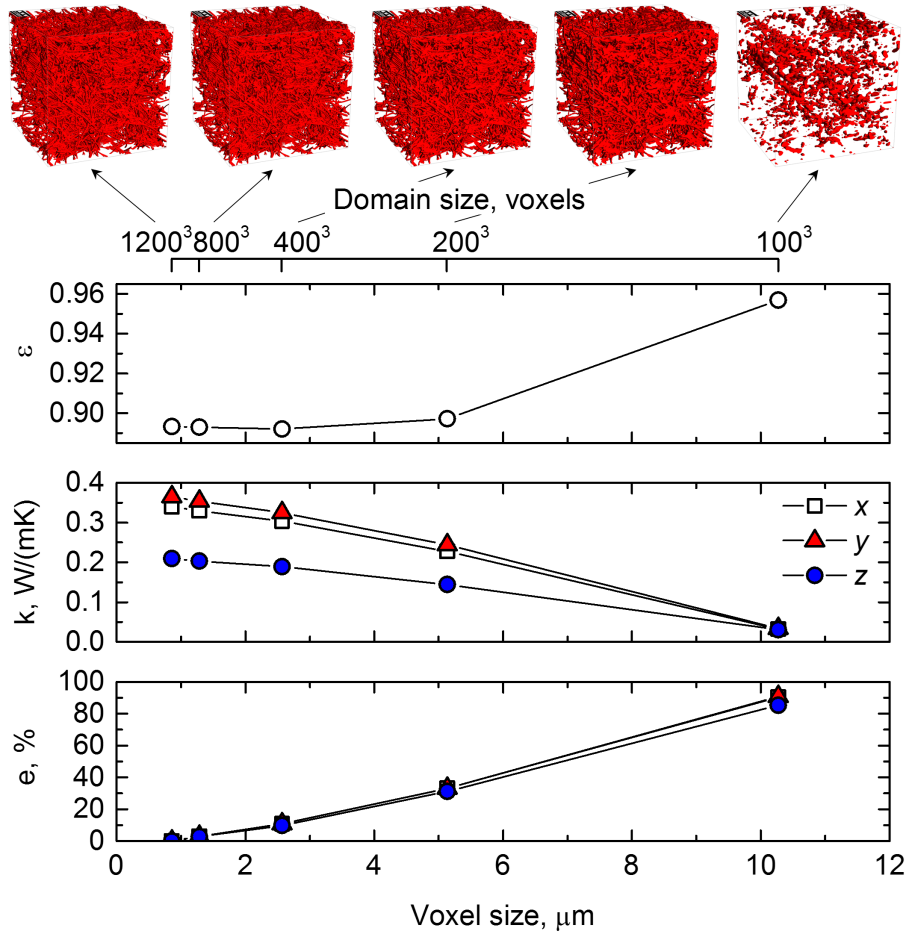


Figure 7. Variation of porosity ε , effective thermal conductivity k and relative error e on the computed thermal conductivity for progressively degraded images.

In order to compare effective properties of the three materials, we performed computations based on the micro-CT of the three substrates with void pores (null conductivity), air- and CO_2 -filled pores, assuming conductivity at 293 K and 1 atm. For the CO_2 case we also computed conductivity at low pressure conditions typical of the early phase of a Martian entry maneuver. In addition, we performed computations with H_2 gas at low pressure (0.01 atm), which is known to be a significant product of the pyrolysis of lightweight phenolic-impregnated ablators [67, 68]. Moreover, H_2 is a major constituent of gas giants' planetary atmospheres (Jupiter, Saturn, Uranus and Neptune).

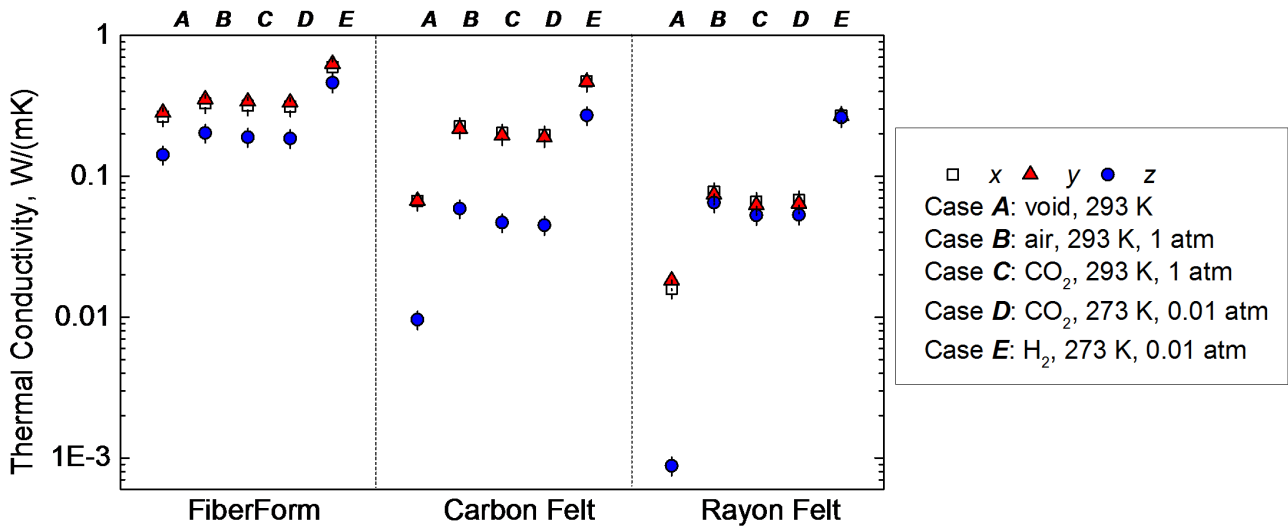


Figure 8. Comparison of room-temperature effective thermal conductivities of rigid and flexible substrates with different pore-filling gas.

The conductivity calculations are summarized in Figure 8. The three materials have lowest thermal conductivity in the through-thickness direction. The results highlight the importance of the gas state within the pores. Due to the effect of the gas conductivity, void pores yield the lowest effective conductivity. The percent difference in conductivity between void pores and gas-filled pores is higher for the higher porosity materials (felts) than FiberForm. For FiberForm, the through-thickness conductivity in CO₂ at standard conditions and CO₂ at low pressure is respectively $\approx 7\%$ and $\approx 10\%$ lower than that in air at standard conditions. In the case of felt, the difference between air and CO₂ conductivities can be up to $\approx 20\%$.

A significant increase of the effective thermal conductivity is observed for the H₂ case. Hydrogen, similarly to other light gases (e.g. helium), has a higher thermal conductivity compared to heavier gases. As a result, the effective thermal conductivity is nearly two to four times higher than that of the low pressure CO₂ case for the in-plane direction and up to six times higher for through-thickness direction. For the rayon felt with H₂, the contrast between the solid and gas phase conductivities becomes so low (≈ 10) that the presence of the gas overwhelms the anisotropy of the solid (in-plane and through-thickness effective conductivities are equivalent). This is an important result that again

highlights the relevance of the gas phase in the thermal behavior of lightweight insulators: even if, in the real case, the radiative conductivity contribution at increasing temperatures might become larger than that of the thermal conductivity [32], the behavior shown in Figure 8 suggests the need of considering the conductivity with actual pore-filling gas mixtures when computing the response of actual TPS materials.

The z direction conductivity of FiberForm is one order of magnitude higher than that of the carbon felt and two orders of magnitude higher than that of the rayon felt. This is due both to the lower porosity and the high connectivity of the material. For the conductivities in the in-plane direction this difference is lower. Indeed, if one considers the thermal-electrical analogy, due to the preferential orientation of the fibers, for the in-plane direction the conductivities of the different phases would nearly behave as resistances in parallel. Hence the effective conductivity would scale as the sum of the conductivities of the different phases. Conversely in the through-the-thickness direction they would behave as resistance in series, where the reciprocal effective conductivity is nearly the sum of the reciprocal conductivities of the single phases.

5. Microscale oxidation simulations

Simulations were performed to investigate the decomposition of carbon fibers due to their interaction with oxygen reactants. The simulations were executed using the PuMA software, described in Ref. [10]. In PuMA, mass diffusion is simulated with random walks of oxygen particles [10, 69]. The carbon/oxygen reactions are modeled using a sticking probability law [10, 69], and the consequent recession of the surfaces is based on a reduction of the gray value of each voxel where a sticking event occurred [10]. After each user-defined number of time steps, the oxidized morphology of the material is segmented using a marching cubes algorithm and rendered with an OpenGL plugin implemented in the PuMA environment.

For the present study, computations were performed on sub-samples of the datasets displayed in Figure 2. We used $400 \times 400 \times 800$ voxels volumes, with a voxel size of 1.29 μm microns.

We assumed simulation parameters (carbon fiber reactivity κ_f and diffusion coefficient D_{ref}) that reproduce both a surface ablation regime and a volume ablation regime. The dimensionless parameter that distinguishes between the two regimes is usually the Thiele number Φ , which is proportional to the ratio κ_f/D_{ref} [10]. At high Thiele number, where the timescale of the oxidation reactions is much smaller than that of the diffusion within the porous medium, the reactants are mostly consumed near the top surface, and the amount of oxygen penetrating in depth is very small. Conversely, at low Thiele number, the diffusion is faster than the chemical reactions and oxidation occurs in depth. The same simulation parameters were used for both FiberForm and carbon felt. This allows a one-to-one comparison of the two materials under the same conditions. It is reasonable to assume the same reactivity for the fibers, as both materials are made of rayon-based carbon fibers, while using the same diffusion coefficient ensures the same oxygen transport. Simulations results are summarized in Figure 9 for $D_{\text{ref}}/\kappa_f \approx 50 \mu\text{m}$ (Figure 9(a) and (a')): diffusion-limited regime, high Thiele number, surface oxidation) and for $D_{\text{ref}}/\kappa_f \approx 2 \text{ mm}$ (Figure 9(b) and (b')): reaction-limited regime, low Thiele number, volume oxidation). The first case simulates typical conditions experienced at the peak heating of a high speed entry trajectory or during high heat flux arcjet testing. Volume ablation condition characterize the late phase of an entry maneuver, at lower TPS material temperatures. The still images of Figure 9 show the time progression of the materials' decomposition due to oxidation. It is observed that at both surface and volume ablation regimes, due to its lower density, the carbon felt ablates much faster than FiberForm. In the surface oxidation regime, we computed a $\sim 35\%$ higher recession rate for carbon felt compared to FiberForm. This is consistent with published arcjet measurements, where the recession of C-PICA was measured to be 14 to 22% higher than that of PICA [1].

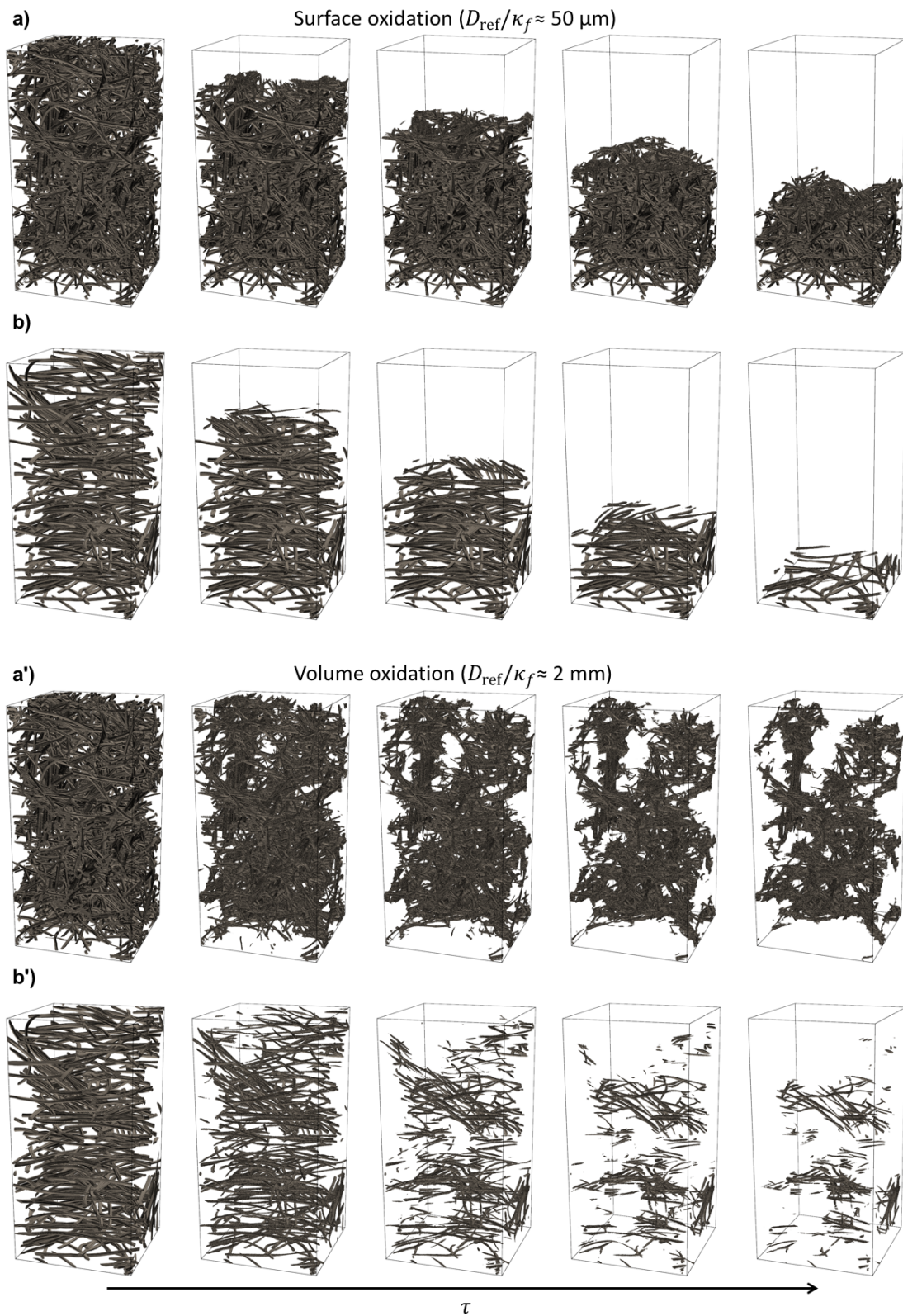


Figure 9. Time progression of a) FiberForm and b) Morgan carbon felt recession simulated with PuMA. a,b) Simulations in diffusion-limited regime, showing surface oxidation, and a',b') simulations in reaction-limited regime, showing volume oxidation.

In order to further address the effect of oxidation on the material performance, effective thermal conductivity simulations – in the simple case of air at standard conditions – were performed on micro-CT volumes oxidized at high Thiele number (volume oxidation). For the diffusion-limited case (surface oxidation), the thickness of the oxidation zone is so small that the material conductivity is not expected to significantly decrease as the material recession progresses. The evolution of the thermal conductivity as a function of normalized porosity for the reaction-limited regime is presented in Figure 10, computed for the volumes shown in Figure 9(b) and (b'). The effective conductivity decreases as the material decomposes and eventually approaches the conductivity of the gas phase k_{gas} .

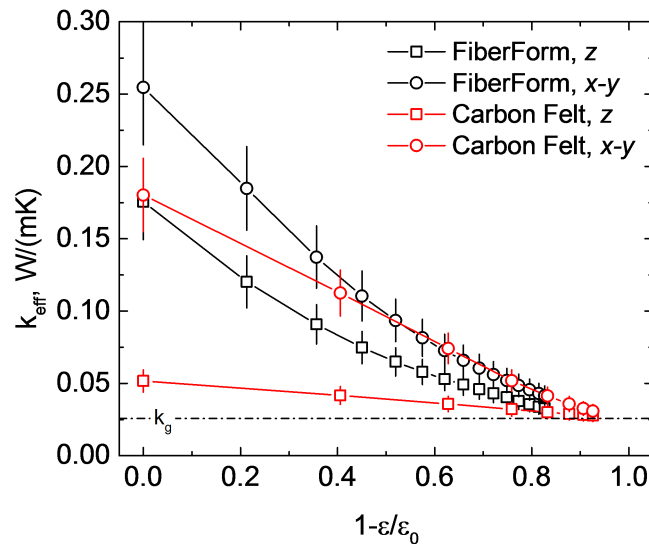


Figure 10. The effective conductivity of both Felt and FiberForm decreases as the material decomposes and approaches the value of the gas thermal conductivity.

It shall be noted that to improve predictions of the effective thermal conductivity for a composite material undergoing physical decomposition, as well as to properly model micro-scale decompositions processes, one should solve the fully coupled process and account, beside the gas phase and material phase conductivities, for the effect of radiative transfer as well as for the energy accommodation of exothermic and endothermic gas/material reactions. The effects of mechanical

decomposition, namely spallation [70], must also be considered. Oxidation is an exothermic process and each reaction event would deposit heat at the surface of the fibers. The heat transfer, both via radiation and conduction, would in turn affect temperature dependent reaction rates, and thereof the oxidation process. Other than a lower density, a different effective conductivity can be an additional cause for the higher decomposition of felts compared to rigid substrates that we observed in Figure 9.

6. Conclusions

We presented a comparison between flexible fibrous felts and a rigid substrate used in the fabrication of carbon/phenolic composites. Microscale oxidation simulations provided evidence that carbon felt recesses faster than rigid FiberForm. A higher recession of C-PICA compared to PICA was observed experimentally in arcjet measurements, and further investigations will be dedicated to address how the substrate decomposition drives the overall ablator performance. The capability of using micro-CT imaging data to compute anisotropic material properties of fibrous insulators has been demonstrated by comparison with reported values from the manufacturers of the materials. We showed that felts have lower room-temperature conductivity than rigid preform, and we highlighted the importance of the conductivity of the pore-filling gas phase for the heat transfer within this class of highly porous preforms. The availability of 3D digital description of the microstructure leads to the possibility of computing the thermal properties at high temperature by simulating radiative heat transfer within the porous medium. Finally, we point to the potential of using Direct Simulation Monte Carlo methods that will enable realistic computations in the rarefied regime using advanced chemistry models for the gas/surface interactions at the fibers surface.

Conflict of interest

None declared.

Acknowledgements

Part of this work was presented at the 8th European Symposium on Aerothermodynamics for Space Vehicle, in Lisbon (Portugal), organized by the European Space Agency. The work was supported by the NASA Entry System Modeling project, by NASA Kentucky EPSCoR Award NNX13AN04A, and by NASA Award NNX14AI97G. The Advanced Light Source is supported by the Director, Office of Science, Office of Basic Energy Sciences, of the U.S. Department of Energy under Contract No. DE-AC02-05CH11231. The authors would like to thank Drs. A. A. McDowell and D. Y. Parkinson for their assistance with x-ray tomography, T. A. Sandstrom for the ray-tracing visualizations and the staff of the Entry Systems and Technology Division at NASA Ames for the several fruitful discussions and constructive comments on the work.

References

- [1] Milos FS, Gasch MJ, Prabhu DK. Conformal Phenolic Impregnated Carbon Ablator Arcjet Testing, Ablation, and Thermal Response. *Journal of Spacecraft and Rockets*. 2015;52(3):804-12.
- [2] Gasch MJ, Stackpoole M, White S, Boghozian T. Development of Advanced Conformal Ablative TPS Fabricated from Rayon- and Pan-Based Carbon Felts. 57th AIAA/ASCE/AHS/ASC Structures, Structural Dynamics, and Materials Conference, 2016.
- [3] Tran H, Johnson C, Rasky D, Hui F, Hsu M-T, Chen Y. Phenolic Impregnated Carbon Ablators (PICA) for Discovery class missions. 31st Thermophysics Conference, 1996. AIAA 1996-11.
- [4] Lu WY, Antoun BR, Korellis JS, Scheffel S, Lee MY, Hardy RD, et al. Material Characterization of Shuttle Thermal Protection System for Impact Analyses. *Journal of Spacecraft and Rockets*. 2005;42(5):795-803.
- [5] Szalai C, Slimko E, Hoffman P. Mars Science Laboratory Heatshield Development, Implementation, and Lessons Learned. *Journal of Spacecraft and Rockets*. 2014;51(4):1167-73.

- [6] Stackpoole M, Sepka SA, Cozmuta I, Kontinos DA. Post-Flight Evaluation of Stardust Sample Return Capsule Forebody Heatshield Material. 46th AIAA Aerospace Sciences Meeting and Exhibit, 2008. AIAA 2008-1202.
- [7] Lachaud J, Cozmuta I, Mansour NN. Multiscale Approach to Ablation Modeling of Phenolic Impregnated Carbon Ablators. *Journal of Spacecraft and Rockets*. 2010;47(6):910-21.
- [8] Borner A, Panerai F, Mansour NN. High temperature permeability of fibrous materials using direct simulation Monte Carlo. *International Journal of Heat and Mass Transfer*.
- [9] Panerai F, White JD, Cochell TJ, Schroeder OM, Mansour NN, Wright MJ, et al. Experimental measurements of the permeability of fibrous carbon at high-temperature. *International Journal of Heat and Mass Transfer*. 2016;101:267-73.
- [10] Ferguson JC, Panerai F, Lachaud J, Martin A, Bailey SCC, Mansour NN. Modeling the oxidation of low-density carbon fiber material based on micro-tomography. *Carbon*. 2016;96:57-65.
- [11] Salvo L, Cloetens P, Maire E, Zabler S, Blandin JJ, Buffière JY, et al. X-ray micro-tomography an attractive characterisation technique in materials science. *Nuclear Instruments and Methods in Physics Research Section B: Beam Interactions with Materials and Atoms*. 2003;200:273-86.
- [12] Landis EN, Keane DT. X-ray microtomography. *Materials Characterization*. 2010;61(12):1305-16.
- [13] Maire E. X-Ray Tomography Applied to the Characterization of Highly Porous Materials. *Annual Review of Materials Research*. 2012;42:163-78.
- [14] Maire E, Withers PJ. Quantitative X-ray tomography. *International Materials Reviews*. 2014;59(1):1-43.
- [15] Torquato S. Random heterogeneous materials: microstructure and macroscopic properties.

Springer Science & Business Media 2013.

- [16] Torquato S. Modeling of physical properties of composite materials. *International Journal of Solids and Structures*. 2000;37(1–2):411-22.
- [17] Whitaker S. *The method of volume averaging*. Springer Science & Business Media 1998.
- [18] Wang M, Pan N. Predictions of effective physical properties of complex multiphase materials. *Materials Science and Engineering: R: Reports*. 2008;63(1):1-30.
- [19] Coindreau O, Vignoles GL. Assessment of geometrical and transport properties of a fibrous C/C composite preform using x-ray computerized micro-tomography: Part I. Image acquisition and geometrical properties. *Journal of materials research*. 2005;20(09):2328-39.
- [20] Vignoles GL, Coindreau O, Ahmadi A, Bernard D. Assessment of geometrical and transport properties of a fibrous C/C composite preform as digitized by x-ray computerized microtomography: Part II. Heat and gas transport properties. *Journal of materials research*. 2007;22(06):1537-50.
- [21] Petrasch J, Schrader B, Wyss P, Steinfeld A. Tomography-Based Determination of the Effective Thermal Conductivity of Fluid-Saturated Reticulate Porous Ceramics. *Journal of Heat Transfer*. 2008;130(3):032602-.
- [22] Thoemen H, Walther T, Wiegmann A. 3D simulation of macroscopic heat and mass transfer properties from the microstructure of wood fibre networks. *Composites Science and Technology*. 2008;68(3–4):608-16.
- [23] Haussener S, Lipiński W, Petrasch J, Wyss P, Steinfeld A. Tomographic Characterization of a Semitransparent-Particle Packed Bed and Determination of its Thermal Radiative Properties. *Journal of Heat Transfer*. 2009;131(7):072701-.
- [24] Haussener S, Coray P, Lipiński W, Wyss P, Steinfeld A. Tomography-based heat and mass transfer characterization of reticulate porous ceramics for high-temperature processing. *Journal of*

Heat Transfer. 2010;132(2):023305.

- [25] Pfrang A, Veyret D, Sieker F, Tsoitridis G. X-ray computed tomography of gas diffusion layers of PEM fuel cells: Calculation of thermal conductivity. *International Journal of Hydrogen Energy*. 2010;35(8):3751-7.
- [26] Calonne N, Flin F, Morin S, Lesaffre B, du Roscoat SR, Geindreau C. Numerical and experimental investigations of the effective thermal conductivity of snow. *Geophysical Research Letters*. 2011;38(23):n/a-n/a.
- [27] Ranut P, Nobile E, Mancini L. High resolution X-ray microtomography-based CFD simulation for the characterization of flow permeability and effective thermal conductivity of aluminum metal foams. *Experimental Thermal and Fluid Science*. 2015;67:30-6.
- [28] Fan X, Ou X, Xing F, Turley GA, Denissenko P, Williams MA, et al. Microtomography-based numerical simulations of heat transfer and fluid flow through β -SiC open-cell foams for catalysis. *Catalysis Today*. 2016;278, Part 2:350-60.
- [29] Vignoles GL. A hybrid random walk method for the simulation of coupled conduction and linearized radiation transfer at local scale in porous media with opaque solid phases. *International Journal of Heat and Mass Transfer*. 2016;93:707-19.
- [30] Bresson G, Ahmadi-Sénichault A, Caty O, Ayvazyan V, Gregori ML, Costa SF, et al. Thermographic and tomographic methods for tridimensional characterization of thermal transfer in silica/phenolic composites. *Composites Part B: Engineering*. 2016;104:71-9.
- [31] Vignoles GL, Ortona A. Numerical study of effective heat conductivities of foams by coupled conduction and radiation. *International Journal of Thermal Sciences*. 2016;109:270-8.
- [32] Nouri N, Panerai F, Tagavi KA, Mansour NN, Martin A. Evaluation of the anisotropic radiative conductivity of a low-density carbon fiber material from realistic microscale imaging. *International Journal of Heat and Mass Transfer*. 2016;95:535-9.

- [33] Zafari M, Panjepour M, Davazdah Emami M, Meratian M. Microtomography-based numerical simulation of fluid flow and heat transfer in open cell metal foams. *Applied Thermal Engineering*. 2015;80:347-54.
- [34] Spanne P, Thovert J, Jacquin C, Lindquist W, Jones K, Adler P. Synchrotron computed microtomography of porous media: topology and transports. *Physical Review Letters*. 1994;73(14):2001.
- [35] Auzeais F, Dunsmuir J, Ferreol B, Martys N, Olson J, Ramakrishnan T, et al. Transport in sandstone: a study based on three dimensional microtomography. *Geophysical Research Letters*. 1996;23(7):705-8.
- [36] Seright R, Liang J, Lindquist WB, Dunsmuir JH. Use of X-ray computed microtomography to understand why gels reduce relative permeability to water more than that to oil. *Journal of Petroleum Science and Engineering*. 2003;39(3):217-30.
- [37] Bernard D, Nielsen Ø, Salvo L, Cloetens P. Permeability assessment by 3D interdendritic flow simulations on microtomography mappings of Al–Cu alloys. *Materials Science and Engineering: A*. 2005;392(1–2):112-20.
- [38] Liu J, Regenauer-Lieb K, Hines C, Liu K, Gaede O, Squelch A. Improved estimates of percolation and anisotropic permeability from 3-DX-ray microtomography using stochastic analyses and visualization. *Geochemistry, Geophysics, Geosystems*. 2009;10(5).
- [39] Degruyter W, Burgisser A, Bachmann O, Malaspinas O. Synchrotron X-ray microtomography and lattice Boltzmann simulations of gas flow through volcanic pumices. *Geosphere*. 2010;6(5):470-81.
- [40] Zermatten E, Haussener S, Schneebeili M, Steinfeld A. Tomography-based determination of permeability and Dupuit–Forchheimer coefficient of characteristic snow samples. *Journal of Glaciology*. 2011;57(205):811-6.

- [41] Gouze P, Luquot L. X-ray microtomography characterization of porosity, permeability and reactive surface changes during dissolution. *Journal of Contaminant Hydrology*. 2011;120–121:45-55.
- [42] Noiriél C. Resolving Time-dependent Evolution of Pore-Scale Structure, Permeability and Reactivity using X-ray Microtomography. *Reviews in Mineralogy and Geochemistry*. 2015;80(1):247-85.
- [43] Soulaine C, Gjetvåg F, Garing C, Roman S, Russian A, Gouze P, et al. The Impact of Sub-Resolution Porosity of X-ray Microtomography Images on the Permeability. *Transport in Porous Media*. 2016;113(1):227-43.
- [44] White C, Scanlon TJ, Brown RE. Permeability of Ablative Materials Under Rarefied Gas Conditions. *Journal of Spacecraft and Rockets*. 2015;53(1):134-42.
- [45] Promentilla MAB, Sugiyama T, Hitomi T, Takeda N. Quantification of tortuosity in hardened cement pastes using synchrotron-based X-ray computed microtomography. *Cement and Concrete Research*. 2009;39(6):548-57.
- [46] Coindreau O, Mulat C, Germain C, Lachaud J, Vignoles GL. Benefits of X-Ray CMT for the Modeling of C/C Composites. *Advanced Engineering Materials*. 2011;13(3):178-85.
- [47] Mansour NN, Panerai F, Martin A, Parkinson DY, MacDowell AA, Fast A, et al. A new approach to light-weight ablators analysis: from micro-tomography measurements to statistical analysis and modeling. 44th AIAA Thermophysics Conference, 2013. AIAA 2013-768.
- [48] Shanti NO, Chan VWL, Stock SR, De Carlo F, Thornton K, Faber KT. X-ray micro-computed tomography and tortuosity calculations of percolating pore networks. *Acta Materialia*. 2014;71:126-35.
- [49] Cooper SJ, Bertei A, Shearing PR, Kilner JA, Brandon NP. TauFactor: An open-source application for calculating tortuosity factors from tomographic data. *SoftwareX*.

- [50] MacDowell AA, Parkinson DY, Haboub A, Schaible E, Nasiatka JR, Yee CA, et al. X-ray micro-tomography at the Advanced Light Source. *Developments in X-Ray Tomography VIII*.
- [51] Dierick M, Masschaele B, Hoorebeke LV. Octopus, a fast and user-friendly tomographic reconstruction package developed in LabView[®]. *Measurement Science and Technology*. 2004;15(7):1366.
- [52] Schindelin J, Arganda-Carreras I, Frise E, Kaynig V, Longair M, Pietzsch T, et al. Fiji: an open-source platform for biological-image analysis. *Nat Methods*. 2012;9(7):676-82.
- [53] Kajiya JT. The rendering equation. *SIGGRAPH Comput Graph*. 1986;20(4):143-50.
- [54] Wiegmann A, Zemitis A. EJ-HEAT: A Fast Explicit Jump Harmonic Averaging Solver for the Effective Heat Conductivity of Composite Materials. Kaiserslautern, Germany: Fraunhofer Institute ITWM; 2006.
- [55] Velichko A, Wiegmann A, Mücklich F. Estimation of the effective conductivities of complex cast iron microstructures using FIB-tomographic analysis. *Acta Materialia*. 2009;57(17):5023-35.
- [56] Becker J, Wieser C, Fell S, Steiner K. A multi-scale approach to material modeling of fuel cell diffusion media. *International Journal of Heat and Mass Transfer*. 2011;54(7-8):1360-8.
- [57] Epstein N. On tortuosity and the tortuosity factor in flow and diffusion through porous media. *Chemical Engineering Science*. 1989;44(3):777-9.
- [58] Cunnington GR, Lee SC. Radiative properties of fibrous insulations - Theory versus experiment. *Journal of Thermophysics and Heat Transfer*. 1996;10(3):460-6.
- [59] Van Eekelen AJ, Lachaud J. Numerical Validation of an Effective Radiation Heat Transfer Model for Fiber Preforms. *Journal of Spacecraft and Rockets*. 2011;48(3):534-7.
- [60] Daryabeigi K, Cunnington GR, Knutson JR. Heat Transfer Modeling for Rigid High-Temperature Fibrous Insulation. *Journal of Thermophysics and Heat Transfer*. 2013;27(3):414-21.
- [61] Nouri N, Martin A. Three dimensional radiative heat transfer model for the evaluation of the

anisotropic effective conductivity of fibrous materials. *International Journal of Heat and Mass Transfer*. 2015;83:629-35.

- [62] Scoggins JB, Magin TE. Development of Mutation++: multicomponent thermodynamic and transport properties for ionized plasmas written in C++. 11th AIAA/ASME Joint Thermophysics and Heat Transfer Conference, 2014. AIAA 2014-966.
- [63] Scoggins JB, Magin TE. Gibbs function continuation for linearly constrained multiphase equilibria. *Combustion and Flame*. 2015;162(12):4514-22.
- [64] Warner SB. *Fiber Science*. Englewood Cliffs: Prentice-Hall; 1995.
- [65] Morton WE, Hearle JWS. *Physical properties of textile fibres*. Fourth ed. Cambridge, England: Woodhead Publishing Limited; 2008.
- [66] Pradere C, Batsale JC, Goyh n che JM, Pailler R, Dilhaire S. Thermal properties of carbon fibers at very high temperature. *Carbon*. 2009;47(3):737-43.
- [67] Wong H-W, Peck J, Assif J, Panerai F, Lachaud J, Mansour NN. Detailed analysis of species production from the pyrolysis of the Phenolic Impregnated Carbon Ablator. *Journal of Analytical and Applied Pyrolysis*.
- [68] Wong H-W, Peck J, Bonomi RE, Assif J, Panerai F, Reinisch G, et al. Quantitative determination of species production from phenol-formaldehyde resin pyrolysis. *Polymer Degradation and Stability*. 2015;112:122-31.
- [69] Lachaud J, Vignoles GL. A Brownian motion technique to simulate gasification and its application to C/C composite ablation. *Computational Materials Science*. 2009;44(4):1034-41.
- [70] Martin A, Bailey SCC, Panerai F, Davuluri RSC, Zhang H, Vazsonyi AR, et al. Numerical and experimental analysis of spallation phenomena. *CEAS Space Journal*. 2016:1-8.